www.sciencemag.org/content/359/6380/1127/suppl/DC1

Supplementary Materials for

A liquid-liquid transition in supercooled aqueous solution related to the HDA-LDA transition

Sander Woutersen,* Bernd Ensing, Michiel Hilbers, Zuofeng Zhao, C. Austen Angell*

*Corresponding author. Email: s.woutersen@uva.nl (S.W.); austenangell@gmail.com (C.A.A.)

Published 9 March 2018, *Science* **359**, 1127 (2018)
DOI: 10.1126/science.aao7049

This PDF file includes:

Materials and Methods
Supplementary Text
Figs. S1 to S8
Table S1
References and Notes

Materials and Methods

Sample preparation

A typical preparation would be as follows: a 10 ml reagent tube with NS14/23 connection is cleaned, rinsed and dried by heating with a heat gun and subsequently cooled with a stream of dry nitrogen. The tube is filled with argon, stoppered and tared. Ca. 0.2 ml of $N_2D_4.D_2O$ is added, the tube stoppered and the exact weight of the hydrazine (no density known) is determined. The calculated amount of TFA-d (d=1.493) is then added slowly at 0 °C under a stream of dry nitrogen. The required dilution is obtained by adding the appropriate amount of D_2O (and optionally H_2O), taking into account the D_2O already present from the hydrazine. The samples are then stored and handled under argon.

To prepare samples for the IR experiments, we squash a droplet of the appropriate volume (approximately 1 microliter) between two 2 mm thick CaF_2 windows separated by a ~25 micron spacer, making sure that the liquid is not in contact with the spacer. The sample thickness (and hence the volume of liquid) is determined by the requirement that the liquid is sufficiently transparent in the IR (hence, much larger than microliter volumes cannot be studied). We found that using ~10 times smaller volumes gives identical results (apart from an overall vertical scaling factor in the IR spectra due to the smaller IR absorption of the thinner liquid layer). The squashed droplet (of which the meniscus can be seen in Fig. 2A) can freely expand or shrink in the transverse direction because there is a ring of air between the outer circumference of the squashed droplet and the inner circumference of the spacer (the latter is outside the photo in Fig. 2A). The droplets have a volume of ~1 microliter. Such microliter volumes (which correspond to $>10^{19}$ molecules) are known to behave as bulk water, in particular from heat capacity measurements in which microliter volumes and volumes as large as 10ml were found to behave exactly the same. The ~25 micrometer-thick layers of water that we prepare from the microliter volumes have properties that are bulk-like, see Ref. (*35*), in which water and ice layers of 2.5 μm (about ten times thinner than ours) were used, without any change in the properties. Surface-sensitive vibrational spectroscopy and ab initio MD simulations (*36, 37*) confirm this: they show that the effect of the interface on the water structure extends <1 nm into the liquid, so the interface effects are negligible in the case of a ~25 μm layer.

Cryogenic FTIR measurements

The sample is mounted in a brass holder in thermal contact with the heat exchanger of a liquid-N_2 cryostat (DN1704, Oxford Instruments). To monitor the temperature a type K thermocouple is mounted close to the sample. To determine the temperature difference between this thermocouple and the inside of the sample cell we preformed calibration measurements in which the solution was replaced by a second thermocouple, see Supplementary text S2 below. Temperature scans were made using an Oxford Instruments ITC4 temperature controller. The time dependence of the temperature was measured using a temperature logger (TC-08 Thermocouple data logger, PicoLog) during all measurements. Graphs of the time-dependent temperatures are shown in Fig. S2. We corrected for small baseline fluctuations in the FTIR spectrum by subtracting the baseline recorded at 4000cm^{-1} (where the sample absorption is negligible) separately for each

FTIR measurement. The infrared spectra were recorded approximately every 18 seconds using a Perkin Spectrum Two FTIR spectrometer (spectral resolution 1 cm^{-1}).

Molecular Dynamics simulations

We have performed classical molecular dynamics (MD) simulations of N_2H_5TFA (160 molecules) in water (840 molecules) in a cubic box subject to periodic boundary conditions. The water molar fraction is thus $x = 0.84$, and equals that of the experiments. The Amber GAFF force field together with the flexible TIP3P water model was used to describe the intra- and intermolecular interactions, with atomic RESP charges obtained from quantum chemical calculations at the HF/6-31G(d) level of theory, following the standard GAFF procedure. The Avogadro and Packmol programs were used to setup the initial configuration, which was relaxed and equilibrated in the NPT ensemble at $T = 300$ K and $p = 1$ atm. We performed a 2 ns NVT production run, saving positions every 1 ps, for analysis. The temperature was controlled with a csvr thermostat with a period of 0.1 ps. The MD simulations were performed with the LAMMPS package(*38*). We also performed 6 ns simulations of pure water (1000 molecules) at different pressures (1, 1000, and 6000 bar) for comparison of the structure of the liquids. In addition, we have performed a short, 10 ps, *ab initio* (density functional theory) molecular dynamics (DFT-MD) simulation of the mixture, as a verification of the forcefield MD simulations. This system contained 8 N_2H_5TFA and 42 water molecules in a cubic box with an edge of L=13.4151A, which was pre-equilibrated with an NPT and an NVT force-field MD simulation of 1 ns each. We used the BLYP exchange correlation functional (*39, 40*), augmented by Grimme's D3 parameterized van der Waals correction (*41*). The DFT-MD simulations were carried out with the CP2K software (*42*), using the combined Gaussian and plane-wave implementation of DFT. The valence electron functions were expanded in a TZV2P Gaussian basis set and a plane wave expansion cutoff at 400 Ry. The nuclei and core electrons were modeled with the norm-conserving pseudopotentials of Goedecker et al. (*43*). The last 5 ps of the DFT-MD simulation were used for analysis.

Supplementary Text

S1. Density jump at the LL transition

In the text we noted that, at the highest water content, 84.4 mol%, where the sharp transition of the present work occurs, the density anomaly could unfortunately not be studied. The inability to observe the density jump in the high water content case was due to the orders-of- magnitude larger size of the sample needed for the density measurement, and the consequent increase in ice nucleation probability that developed before the L-L transition temperature was reached (the nucleation probability increases exponentially with volume). In a microscopic density measurement, we expect that, at the transition, a sharp jump in sample volume would be observed. However, due to the high effective pressure in the solution sample, the density jump should be smaller than that observed between LDA and HDA water by Mishima (*44*). Such a study is part of our future work plan.

S2. Temperature read-out

All IR data in the main text is presented with temperature values as read out during the IR scans by a thermocouple connected to a point on the brass sample holder that keeps together the two CaF_2 windows and the Teflon spacer and the liquid droplet between them. The thermocouple was connected to a point as close as possible to the liquid layer. To estimate the actual temperature *inside* the liquid layer, we performed separate measurements in which we replaced the liquid sample by a second thermocouple squeezed between the two CaF_2 windows (thus replacing the liquid layer), using thermal paste to ensure good thermal contact between the thermocouple and the windows, and measured the difference between the two thermocouples, see Figure S3. These results indicate that for temperature-scanning rates comparable to the ones used in the IR measurements of Fig. 2B-E, at 200K the temperature in the cell is several K higher than at the probe thermocouple. The difference in readout and sample temperature is different during cooling and heating. This hysteresis difference is ~1 K for slow scan rates. This means that the ~3 K hysteresis in Fig. 2G is partly due to the thermocouple not being in direct contact with the liquid.

S3. Background absorption due to deuterated molecular species in the sample

The spectra shown in Figures 2 and 4 of the main text are dominated by the absorption of the OH-stretching mode of HDO. To determine the background absorption due to deuterated species, we need the spectrum of a fully deuterated ($N_2D_5CF_3COO$ in D_2O) solution. However, it was not possible to prepare such a solution with a sufficient isotopic purity for this purpose, because (i) the starting compounds for preparing $N_2D_5CF_3COO$ already contain a small amount of H [the CF_3COOD is specified as >99.5%D (Sigma Aldrich), the $N_2D_4{\cdot}D_2O$ as >99.2%D (Cambridge Isotopes)], and (ii) although the sample was prepared under N_2 atmosphere, we cannot exclude a small amount of H/D exchange during the preparation and subsequent handling of the solution (this exchange might be with atmospheric water and/or OH groups in the glassware).

To determine the IR spectrum of a completely deuterated solution we therefore proceeded as follows. We prepared a "spiked" solution, in which a small fraction of the D_2O was replaced by H_2O, and compared the IR spectra in the presence and absence of the "OH-spiking", see Figure S4. To determine the OH fraction in the non-spiked sample we used proton-NMR spectroscopy: we added 3.6 mg acetronitrile to 561.3 mg solution as internal calibrant, and used the integrated water-proton and acetonitrile-proton peaks to determine the OH-fraction x_H. From this value and the known amount of added H_2O (determined using an analytical balance), the x_H of the spiked sample could be calculated.

Using the spiked and non-spiked IR spectra and x_H values, we could determine the spectrum of a pure OD solution. Both spectra are linear combinations of the isotope-species spectra:

$$A_{sample}(\nu, x_H) = (1-x_H)A_D(\nu) + x_H A_H(\nu),$$

so a linear combination of the two spectra with the appropriate coefficients gives us $A_D(\nu)$. The resulting 100%D spectrum, shown as the grey curve the graph, has negligible absorbance in the frequency region shown in Figures 2 and 4 of the main text. The residual ~0.05 OD signal is mostly due to the (frequency-independent) reflection losses at

the four CaF_2 surfaces of the sample cell. The narrow peak at 3100 cm^{-1} is the overtone of the anti-symmetric CO-stretch mode of CF_3COO^-.

S4. Comparing the hydrogen-bond coordination numbers in the ionic solution and neat water

In Figure S6 and S7, we show the radial H…O and O…H radial distribution functions (RDF) of neat water and of our ionic solution (also shown in Fig. 3B of the main text) together with their integrals, and integrals of Gaussian fits to the first peak. The hydrogen-bond coordination number of a water molecule can be determined either from the integral of the Gaussian fit to the first peak of the RDF or from the integral of the RDF to its first minimum [the reason for integrating the Gaussian fit (rather than integrating the RDF up to its first minimum) is that the RDF is not zero at its first minimum because of overlap between the first and second peak, so an integral of the raw data might overestimate the hydrogen-bond coordination number].

From these integrals, which are given in Table S1, the average hydrogen-bond coordination number of a water molecule can be estimated by adding the O...H integral and 2 times the H…O integral (since each water molecule contains one O and two H atoms). In the case of the ionic solution, these H…O and O...H integrals are themselves sums of the water...water and water...ion integrals (these sums are given in separate lines in the table). In this way, one obtains hydrogen-bond coordination numbers of 3.2 for neat water at ambient pressure, 3.5 for the ionic solution at ambient pressure, and 3.3 for neat water at 6 kbar when using the Gaussian-fit integrals. When using the integrals to the first minimum of the RDF, one obtains hydrogen-bond coordination numbers of 3.8 for neat water at 1 bar, 4.3 for the ionic solution, and 3.9 for neat water at 6 kbar. These values can be somewhat smaller than 4 due to the dynamic nature of the tetrahedral hydrogen-bond coordination shell. Note that the integrals for the solution average over water molecules that are partly coordinated by ions and water molecules that are fully coordinated by other waters. We can thus conclude that the hydrogen-bond coordination numbers of a water molecule are very similar in the ionic solution and in neat water.

Fig. S1

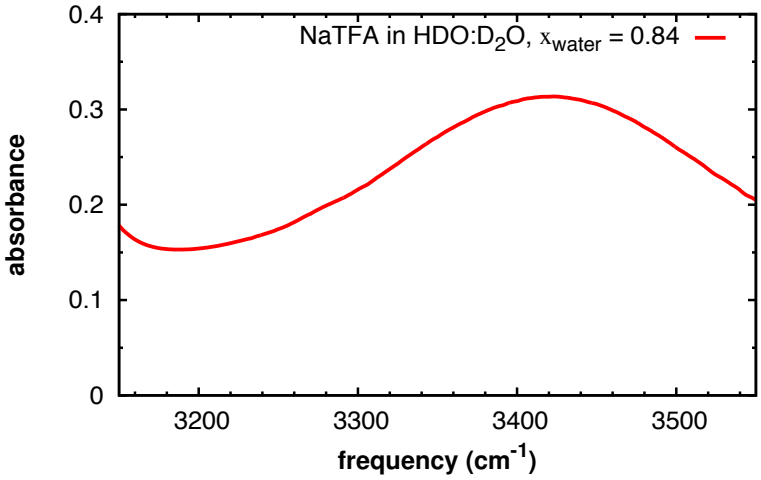

IR spectrum of NaTFA solution in HDO:D_2O. This spectrum shows that the shoulder at ~3300 cm^{-1} observed in Fig. 2B,E of the main text for (N_2HD_4/N_2D_5)TFA in HDO:D_2O is lacking in the spectrum of NaTFA in HDO:D_2O (x_{water} = 0.84). This shoulder can therefore be assigned to (NH-stretching of) $N_2HD_4^+$.

Fig. S2

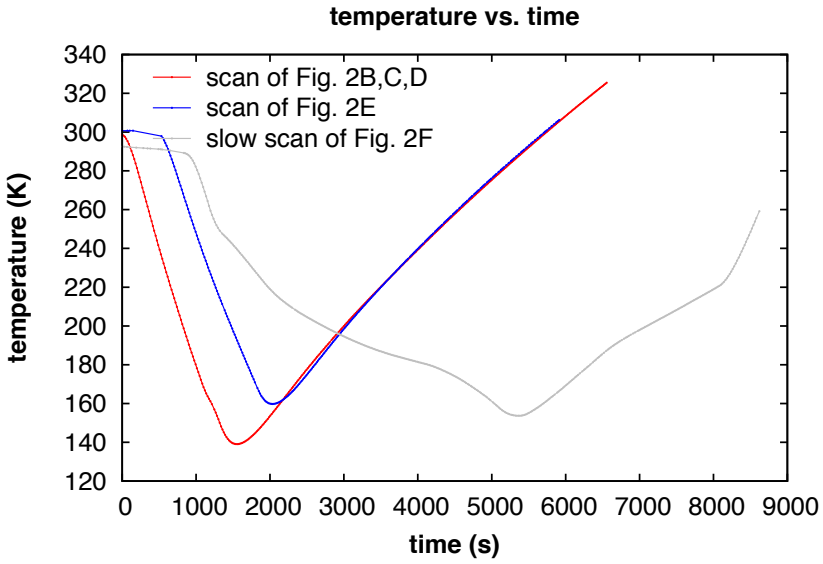

Time dependence of the temperature during the measurements. We cooled down and reheated the liquid samples at different cooling rates. Shown is the temperature of the thermocouple mounted close to the sample vs. time for each of the measurements shown in the main text. Note the identical cooling rates (negative slope) during the measurements of Figs. 2B,C, D and E, and the slower cooling rate (1K/min) at temperatures around 200K in the measurement of Fig 2F,G. In all measurements, we cool the liquid sample down to a temperature well below the liquid-liquid transition temperature and subsequently reheat the liquid sample to confirm that the transition is reversible.

Fig. S3

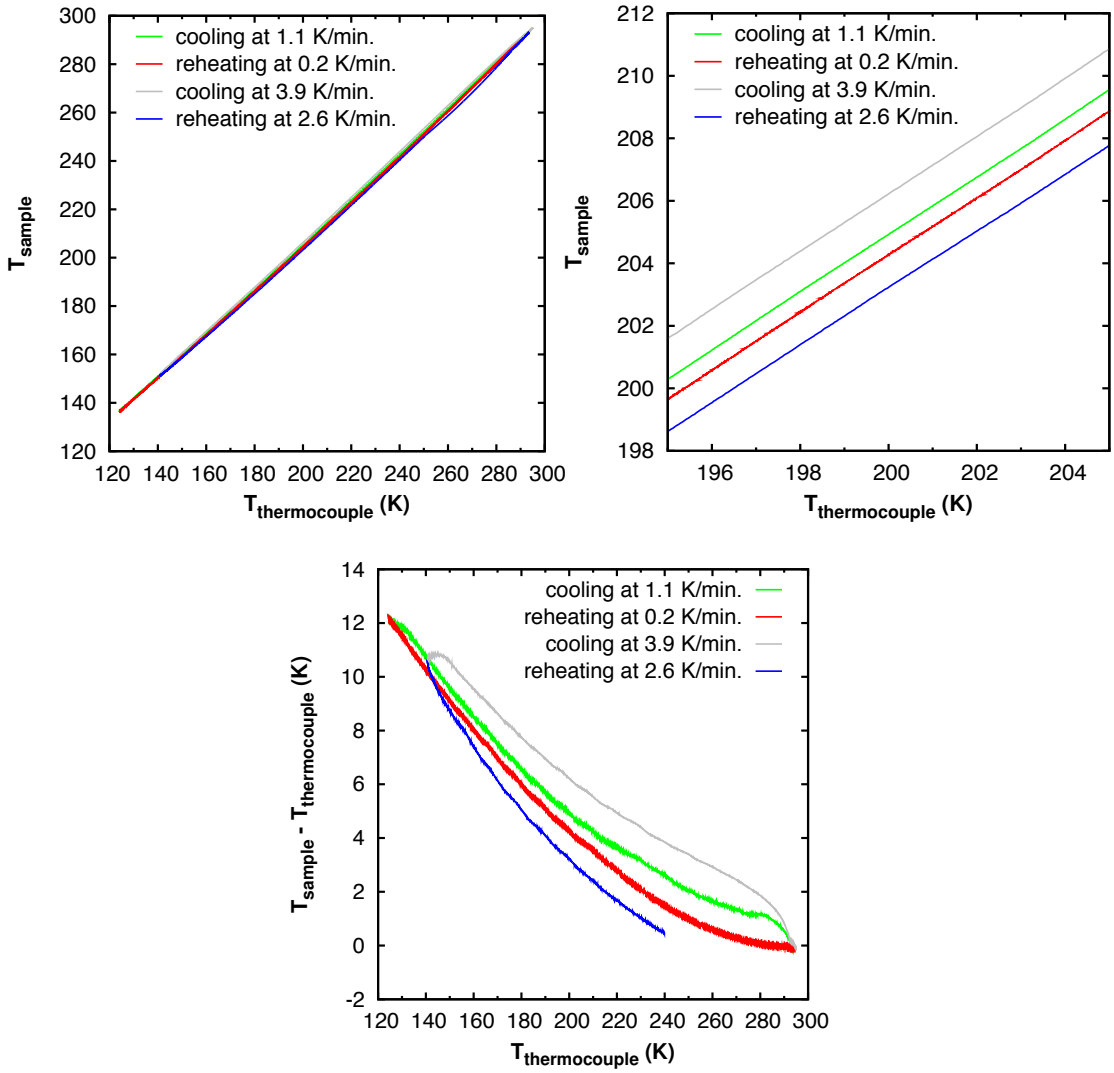

Temperature calibration and temperature hysteresis (see Supplementary text S2). Upper two panels: in a separate set of temperature scans, we replaced the liquid sample by a second thermocouple to measure the temperature difference between the probe-thermocouple readout as used in the IR measurements and the actual temperature inside the (now empty) liquid-sample cell. Lower panel: the temperature difference shows a hysteresis that depends on the scan rate.

Fig. S4

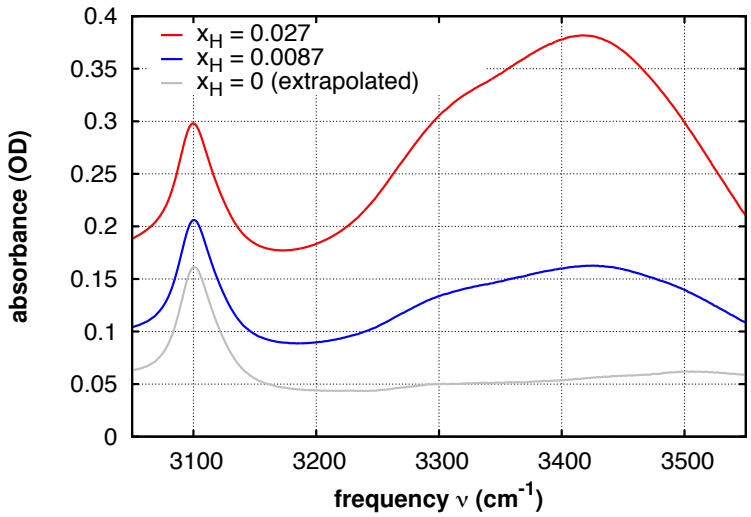

Background absorption of the deuterated solution. IR absorption spectra of $(N_2HD_4/N_2D_5)CF_3COO$:(HDO/D_2O) samples with different H/D ratios. Sample thickness 25 μm. See Supplementary Text S3 for details.

Fig. S5

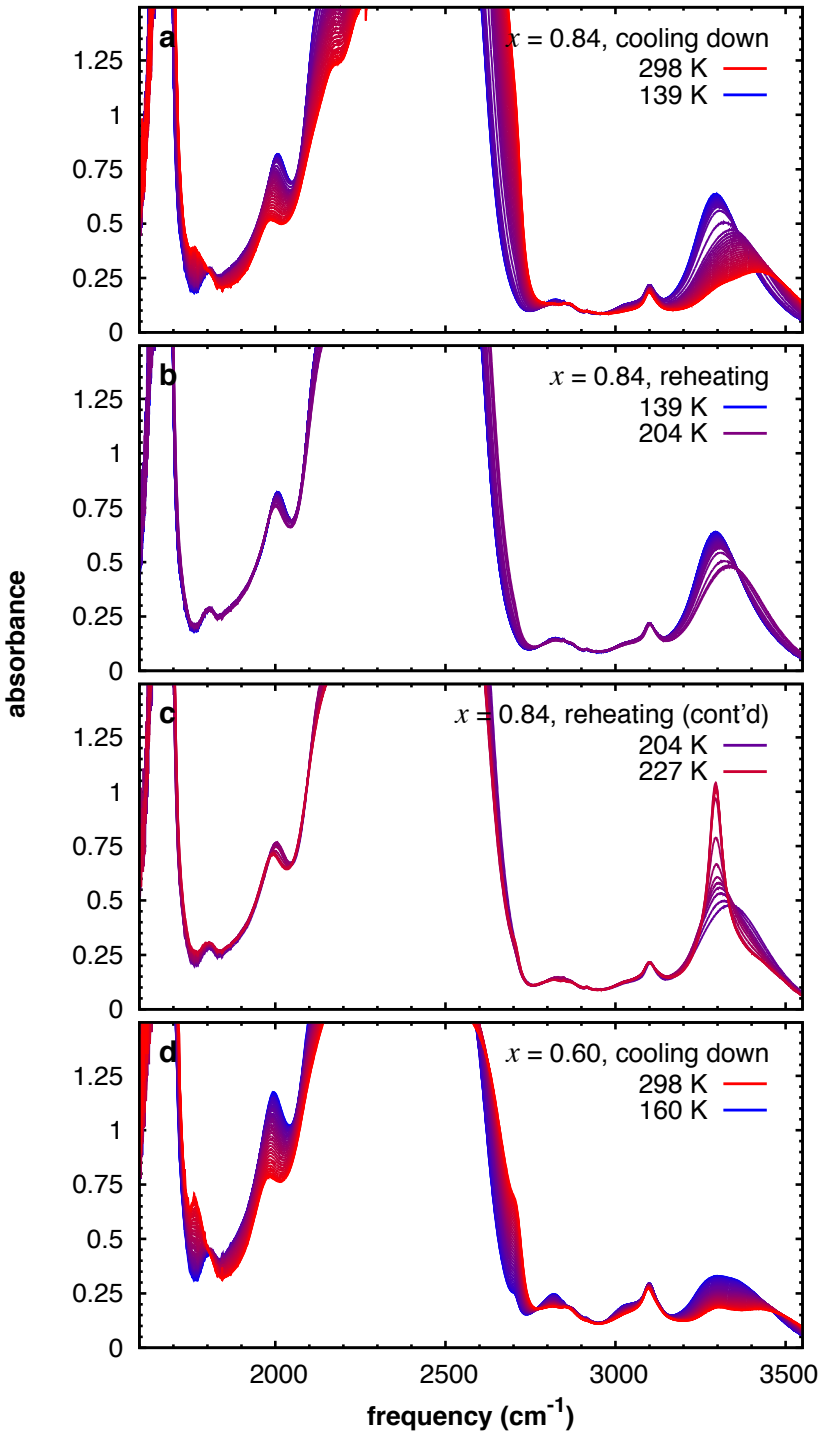

IR spectra with a broader range. The spectra of Fig. 2 in the main text, with extended frequency range. Frequencies below 1600 cm^{-1} were not accessible due to IR absorption by the sapphire outer windows of the cryostat.

Fig. S6

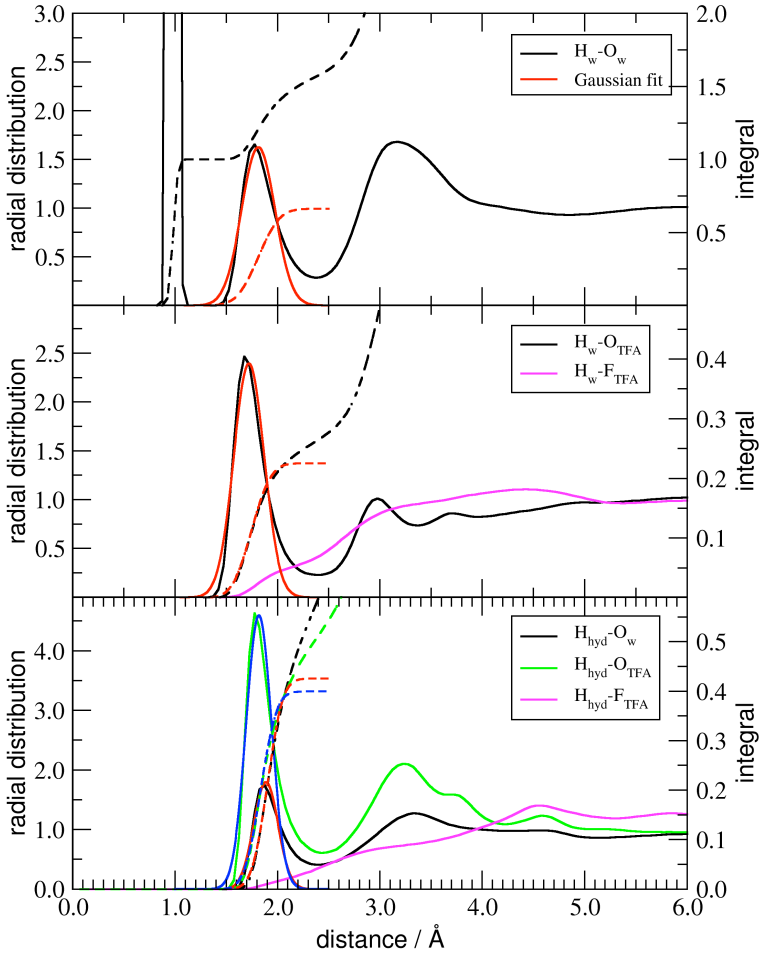

Hydrogen-bond length distributions in hydrazinium-trifluoroacetate solution. Radial distribution of water hydrogens (top and middle panels) and hydrazinium hydrogens (bottom panel) with respect to hydrogen bond acceptor atoms, respectively water oxygens (top panel), trifluoroacetate oxygens (middle panel), and both for hydrazinium hydrogens (bottom panel). In the upper graph the first peak at ~1Å is due to the covalently bonded O atom. The first H…O and O…H hydrogen-bond peaks (centered at a distance of ~1.7Å) are fitted with Gaussians (red and blue curves). The integrals of the Gaussian fits are shown as red and blue dashed lines and refer to the right-hand-side axis.

Fig. S7

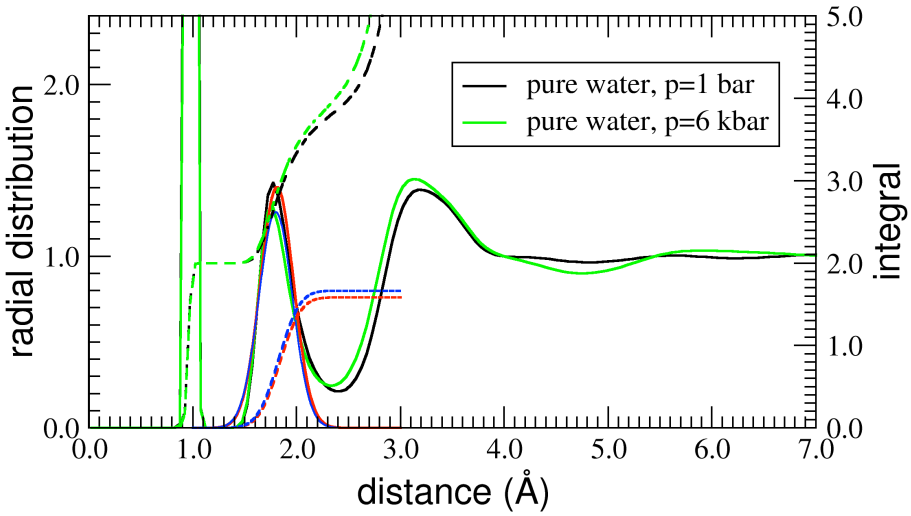

Comparison of the H…O hydrogen-bond length distributions in neat water at ambient and 6 kbar pressure. Radial distribution of water hydrogens with respect to water oxygens in neat water at standard conditions (black and red graphs) and at a pressure of 6 kbar (green and blue curves). The H…O hydrogen-bond peak, centered at a distance of about 1.7 Å, is fitted with a Gaussian (red and blue curves). The integrals of the Gaussian fits are shown as red and blue dashed lines and refer to the right-hand-side axis.

Fig. S8

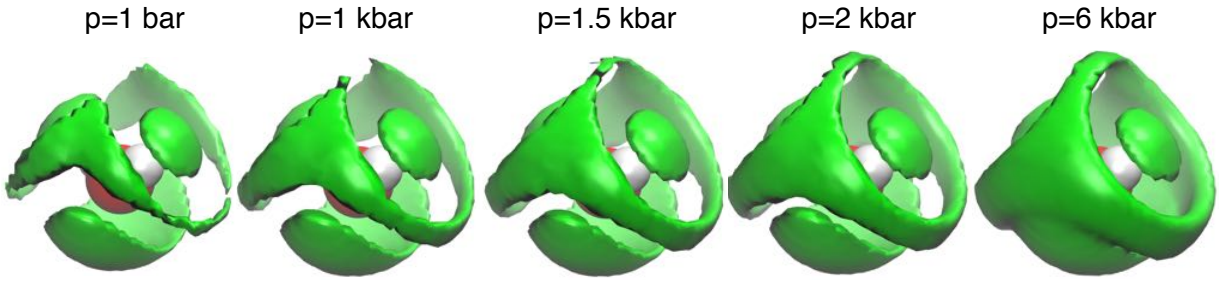

Molecular dynamics simulations of neat water at ambient and elevated pressure. In addition to the 6 kbar pressure simulation of which the result is shown in Fig.3F, we have also carried out simulations at intermediate pressures. These simulations show that the 3D density distribution of water oxygen atoms around a water molecule changes with increasing external pressure. The data were obtained from 5 ns NPT simulations of 1000 fully flexible TIP3P water molecules at a temperature of 300 K. These results show that with increasing pressure the orientational hydrogen-bond distribution function becomes similar to that of the ionic solution at ambient pressure (Fig. 3G).

Table S1

Positions of the first peaks of the O…H and H…O hydrogen-bond radial distribution functions, and integrals of these first peaks. The integrals are taken over a Gaussian function fitted to the first peak, and over the raw data up to the first minimum.

Radial distribution *g*(*r*)	**Peak maximum (Å)**	**Integral of Gaussian fit**	**Integral to 1st minimum**
Neat water, *p* = 1 bar			
$H_{water}…O_{water}$	1.77	0.79	0.94
$O_{water}…H_{water}$	1.77	1.58	1.87
Neat water, *p* = 1 kbar			
$H_{water}…O_{water}$	1.77	0.80	0.95
$O_{water}…H_{water}$	1.77	1.60	1.89
Neat water, *p* = 1.5 kbar			
$H_{water}…O_{water}$	1.76	0.81	0.95
$O_{water}…H_{water}$	1.76	1.61	1.90
Neat water, *p* = 2 kbar			
$H_{water}…O_{water}$	1.76	0.81	0.95
$O_{water}…H_{water}$	1.76	1.62	1.91
Neat water, *p* = 6 kbar			
$H_{water}…O_{water}$	1.76	0.83	0.97
$O_{water}…H_{water}$	1.76	1.67	1.93
Ionic solution, *p* = 1 bar			
$H_{water}…O_{water}$	1.77	0.66	0.79
$H_{water}…O_{TFA}$	1.69	0.23	0.27
Sum($H_{water}…O_{water}$, $H_{water}…O_{TFA}$)		0.89	1.05
$O_{water}…H_{water}$	1.77	1.32	1.57
$O_{water}…H_{hydrazinium}$	1.86	0.41	0.59
Sum($O_{water}…H_{water}$, $O_{water}…H_{hydrazinium}$)		1.73	2.16

References and Notes

1. P. H. Poole, F. Sciortino, U. Essmann, H. E. Stanley, Phase-behavior of metastable water. *Nature* **360**, 324–328 (1992). doi:10.1038/360324a0

2. P. H. Poole, F. Sciortino, T. Grande, H. E. Stanley, C. A. Angell, Effect of hydrogen bonds on the thermodynamic behavior of liquid water. *Phys. Rev. Lett.* **73**, 1632–1635 (1994). doi:10.1103/PhysRevLett.73.1632 Medline

3. M. G. Sceats, S. A. Rice, in *Water: A Comprehensive Treatise*, F. Franks, Ed. (Plenum, 1982), vol. 7, pp. 83–211.

4. H. Kanno, C. A. Angell, Water: Anomalous compressibilities to 1.9 kbar and correlation with supercooling limits. *J. Chem. Phys.* **70**, 4008–4016 (1979). doi:10.1063/1.438021

5. S. Chatterjee, P. G. Debenedetti, Fluid-phase behavior of binary mixtures in which one component can have two critical points. *J. Chem. Phys.* **124**, 154503 (2006). doi:10.1063/1.2188402 Medline

6. M. A. Anisimov, Cold and supercooled water: A novel supercritical-fluid solvent. *Russ. J. Phys. Chem. B* **6**, 861–867 (2012). doi:10.1134/S199079311208009X

7. J. W. Biddle, V. Holten, M. A. Anisimov, Behavior of supercooled aqueous solutions stemming from hidden liquid-liquid transition in water. *J. Chem. Phys.* **141**, 074504 (2014). doi:10.1063/1.4892972 Medline

8. D. G. Archer, R. W. Carter, Thermodynamic properties of the NaCl+H_2O system. 4. Heat capacities of H_2O and NaCl(aq) in cold-stable and supercooled states. *J. Phys. Chem. B* **104**, 8563–8584 (2000). doi:10.1021/jp0003914

9. C. A. Angell, Insights into phases of liquid water from study of its unusual glass-forming properties. *Science* **319**, 582–587 (2008). doi:10.1126/science.1131939 Medline

10. J. Riemenschneider, R. Ludwig, Comment on “Isotope effects in liquid water by infrared spectroscopy. IV. No free OH groups in liquid water”. *J. Chem. Phys.* **135**, 117101 (2011). doi:10.1063/1.3624572 Medline

11. M. Oguni, C. A. Angell, Heat capacities of H_2O + H_2O_2, and H_2O + N_2H_4, binary solutions: Isolation of a singular component for C_p of supercooled water. *J. Chem. Phys.* **73**, 1948–1954 (1980). doi:10.1063/1.440303

12. Z. Zhao, C. A. Angell, Apparent first-order liquid-liquid transition with pre-transition density anomaly, in water-rich ideal solutions. *Angew. Chem. Int. Ed.* **55**, 2474–2477 (2016). doi:10.1002/anie.201510717 Medline

13. W. J. Moore, *Physical Chemistry* (Prentice-Hall, ed. 4, 1972).

14. D. Corradini, M. Rovere, P. Gallo, A route to explain water anomalies from results on an aqueous solution of salt. *J. Chem. Phys.* **132**, 134508 (2010). doi:10.1063/1.3376776 Medline

15. D. Corradini, M. Rovere, P. Gallo, Structural properties of high and low density water in a supercooled aqueous solution of salt. *J. Phys. Chem. B* **115**, 1461–1468 (2011). doi:10.1021/jp1101237 Medline

16. See supplementary materials.

17. K. Murata, H. Tanaka, Liquid-liquid transition without macroscopic phase separation in a water-glycerol mixture. *Nat. Mater.* **11**, 436–443 (2012). doi:10.1038/nmat3271 Medline

18. M. Yang, J. L. Skinner, Signatures of coherent vibrational energy transfer in IR and Raman line shapes for liquid water. *Phys. Chem. Chem. Phys.* **12**, 982–991 (2010). doi:10.1039/B918314K Medline

19. A. K. Wyczalkowska, K. S. Abdulkadirova, M. A. Anisimov, J. V. Sengers, Thermodynamic properties of H_2O and D_2O in the critical region. *J. Chem. Phys.* **113**, 4985–5002 (2000). doi:10.1063/1.1289244

20. C. A. Angell, E. J. Sare, J. Donnella, D. R. MacFarlane, Homogeneous nucleation and glass transition temperatures in solutions of Li salts in D_2O and H_2O. Doubly unstable glass regions. *J. Phys. Chem.* **85**, 1461–1464 (1981). doi:10.1021/j150611a001

21. T. A. Ford, M. Falk, Hydrogen bonding in water and ice. *Can. J. Chem.* **46**, 3579–3586 (1968). doi:10.1139/v68-591

22. K. Fumino, A. Wulf, R. Ludwig, Hydrogen bonding in protic ionic liquids: Reminiscent of water. *Angew. Chem. Int. Ed.* **48**, 3184–3186 (2009). doi:10.1002/anie.200806224 Medline

23. P. G. Debenedetti, H. E. Stanley, Supercooled and glassy water. *Phys. Today* **56**, 40–46 (2003). doi:10.1063/1.1595053

24. A. K. Soper, M. A. Ricci, Structures of high-density and low-density water. *Phys. Rev. Lett.* **84**, 2881–2884 (2000). doi:10.1103/PhysRevLett.84.2881 Medline

25. R. Leberman, A. K. Soper, Effect of high salt concentrations on water structure. *Nature* **378**, 364–366 (1995). doi:10.1038/378364a0 Medline

26. F. Perakis, P. Hamm, Two-dimensional infrared spectroscopy of supercooled water. *J. Phys. Chem. B* **115**, 5289–5293 (2011). doi:10.1021/jp1092288 Medline

27. H. Senapati, K. K. Kadiyala, C. A. Angell, One- and two-step calorimetric studies of crystallization kinetics in simple ionic glass-forming liquids. 1. Calcium nitrate-potassium nitrate system. *J. Phys. Chem.* **95**, 7050–7054 (1991). doi:10.1021/j100171a060

28. This small difference probably originated mainly from the sample temperature lagging behind the temperature of the thermocouple (see fig. S3), which was not immersed in the liquid but attached to the brass holder keeping the CaF_2 windows together.

29. O. Mishima, Y. Suzuki, Propagation of the polyamorphic transition of ice and the liquid-liquid critical point. *Nature* **419**, 599–603 (2002). doi:10.1038/nature01106 Medline

30. A. Shalit, F. Perakis, P. Hamm, Two-dimensional infrared spectroscopy of isotope-diluted low density amorphous ice. *J. Phys. Chem. B* **117**, 15512–15518 (2013). doi:10.1021/jp4053743 Medline

31. A. Shalit, F. Perakis, P. Hamm, Disorder-suppressed vibrational relaxation in vapor-deposited high-density amorphous ice. *J. Chem. Phys.* **140**, 151102 (2014). doi:10.1063/1.4871476

32. P. Gallo, K. Amann-Winkel, C. A. Angell, M. A. Anisimov, F. Caupin, C. Chakravarty, E. Lascaris, T. Loerting, A. Z. Panagiotopoulos, J. Russo, J. A. Sellberg, H. E. Stanley, H. Tanaka, C. Vega, L. Xu, L. G. M. Pettersson, Water: A tale of two liquids. *Chem. Rev.* **116**, 7463–7500 (2016). doi:10.1021/acs.chemrev.5b00750 Medline

33. P. Gallo, H. E. Stanley, Supercooled water reveals its secrets. *Science* **358**, 1543–1544 (2017). doi:10.1126/science.aar3575 Medline

34. K. H. Kim, A. Späh, H. Pathak, F. Perakis, D. Mariedahl, K. Amann-Winkel, J. A. Sellberg, J. H. Lee, S. Kim, J. Park, K. H. Nam, T. Katayama, A. Nilsson, Maxima in the thermodynamic response and correlation functions of deeply supercooled water. *Science* **358**, 1589–1593 (2017). doi:10.1126/science.aap8269 Medline

35. H. Iglev, M. Schmeisser, K. Simeonidis, A. Thaller, A. Laubereau, Ultrafast superheating and melting of bulk ice. *Nature* **439**, 183–186 (2006). doi:10.1038/nature04415 Medline

36. Y. Nagata, R. E. Pool, E. H. G. Backus, M. Bonn, Nuclear quantum effects affect bond orientation of water at the water-vapor interface. *Phys. Rev. Lett.* **109**, 226101 (2012). doi:10.1103/PhysRevLett.109.226101 Medline

37. P. K. Gupta, M. Meuwly, Dynamics and vibrational spectroscopy of water at hydroxylated silica surfaces. *Faraday Discuss.* **167**, 329–346 (2013). doi:10.1039/c3fd00096f Medline

38. S. Plimpton, Fast parallel algorithms for short-range molecular dynamics. *J. Comput. Phys.* **117**, 1–19 (1995). doi:10.1006/jcph.1995.1039

39. A. D. Becke, Density-functional exchange-energy approximation with correct asymptotic behavior. *Phys. Rev. A* **38**, 3098–3100 (1988). doi:10.1103/PhysRevA.38.3098 Medline

40. C. Lee, W. Yang, R. G. Parr, Development of the Colle-Salvetti correlation-energy formula into a functional of the electron density. *Phys. Rev. B* **37**, 785–789 (1988). doi:10.1103/PhysRevB.37.785 Medline

41. S. Grimme, J. Antony, S. Ehrlich, H. Krieg, A consistent and accurate ab initio parametrization of density functional dispersion correction (DFT-D) for the 94 elements H-Pu. *J. Chem. Phys.* **132**, 154104 (2010). doi:10.1063/1.3382344 Medline

42. CP2K Open Source Molecular Dynamics, www.cp2k.org.

43. S. Goedecker, M. Teter, J. Hutter, Separable dual-space Gaussian pseudopotentials. *Phys. Rev. B* **54**, 1703–1710 (1996). doi:10.1103/PhysRevB.54.1703 Medline

44. O. Mishima, Reversible first-order transition between two H_2O amorphs at ~0.2 GPa and ~135 K. *J. Chem. Phys.* **100**, 5910–5912 (1994). doi:10.1063/1.467103